Electronic Supplementary Material (ESI) for Soft Matter.

Supplementary Information

Yielding and Flow of Cellulose Microfibril Dispersions in the Presence of Charged Polymer

Daan W. de Kort[a,b], Sandra J. Veen[c], Henk Van As[a,b], Daniel Bonn[d], Krassimir P. Velikov[c,e], John P.M. van Duynhoven[a,b,c,*]

[a]Laboratory of Biophysics, Wageningen University, Dreijenlaan 3, 6703 HA Wageningen, The Netherlands

[b]TI-COAST, Science Park 904, 1098 XH Amsterdam, The Netherlands

[c]Unilever R&D, Olivier van Noortlaan 120, 3133 AT Vlaardingen, The Netherlands

[d]Van der Waals-Zeeman Institute, IoP, University of Amsterdam, Science Park 904, 1098 XH Amsterdam, The Netherlands

[e]Soft Condensed Matter, Debye Institute for Nanomaterials Science, Utrecht University, Princetonplein 5, 3584 CC Utrecht, The Netherlands

*Corresponding Author

Table of Contents:

S1a. *Microstructural characterization of BCMF/CMC dispersions*

In the presence of CMC, when added in the process of deagglomeration, the distribution of microfibrils over the available volume is more homogeneous, but heterogeneity persists on larger scales due to incomplete deflocculation.[1] CMC is thought to associate with cellulose mainly through hydroxyl-mediated hydrogen bonding. For example, one early study showed that CMC can interfere with the *in vivo* assembly of BC microfibrils (i.e., linear aggregates of cellulose chains)[2], where the degree of substitution (DS) of hydroxyl groups of the CMC chain by carboxymethyl groups plays a critical role.[3] CMC that is not fully substituted with carboxymethyl groups has hydroxyl groups remaining that can, in principle, take part in hydrogen bonding. It is thought that BC microfibril formation is impacted by these hydrogen-bonding interactions.

We investigate the associative behavior of CMC in the dispersions by performing "local" viscosity measurements for which we use ^{19}F–labeled nanoprobes. Their mobility is observed by ^{19}F NMR diffusometry and locally probes the viscosity of the continuous phase.

Experimental procedures

AFM. A 5 µL aliquot of microfibril dispersion was deposited on a silica wafer. The silica wafer was glow-discharged under vacuum before being used to improve the surface hydrophilicity. Afterward, the samples were dried in air, washed with deionized water, and dried again under a nitrogen flow to remove nonadsorbed material. The sample was analyzed with a Bruker Nanoscope V instrument in peak force tapping mode. Here, the AFM tip oscillates in a sinusoidal manner in the vertical direction, while the peak force is used as a feedback signal. This mode allows for direct force control and avoids damage due to lateral forces. Image contrast is provided by the peak force error (the feedback signal). Peak force images offer better resolution than height images, especially for soft samples.[4] Silicon nitride tips with a typical radius of 2 nm (Bruker SCANASYST-AIR) were used for samples in the dilute regime, and silicon nitride tips with a typical radius of 20 nm (Bruker NP-10) were used for samples in the concentrated regime.

Cryo-SEM. A droplet of sample was placed on top of a rivet and plunge-frozen in melting ethane. The sample was cryo-planed using a cryo-ultramicrotome (Leica Ultracut UCT EM UC7/FC7), to obtain a freshly prepared cross-section. Cryo-planing was done first with a section thickness of 100 nm at a speed of 50 mm/s using a glass knife. The last sections were made at decreasing thickness, down to 20 nm, with a speed of 2 mm/s using a diamond knife (Diatome histo cryo 8 mm) at –120 °C. The rivet

was mounted onto a holder and transferred into a Gatan Alto2500 preparation chamber. To reveal microstructures under the planed surface, the temperature of the sample was increased for a short while to –90 °C to remove a thin layer of water by sublimation. This yielded a 3D view of the planed sample. The sample was sputter-coated with platinum (120 s, 10 mA) for a better SEM contrast and to prevent charging by the electron beam. The sample was imaged using a Zeiss Auriga field-emission SEM at –125 °C and an accelerating voltage of 3 kV.

Nanoprobe diffusometry. ^{19}F diffusion-ordered spectroscopy (DOSY) was performed on a Bruker Avance II spectrometer at 7.0 T magnetic field strength (resonance frequency 282 MHz for ^{19}F), equipped with a Bruker diff25 gradient probe (maximum pulsed field gradient intensity 9.60 T/m). The probe was equipped with a 10-mm rf insert tuned to the ^{19}F resonance frequency. Sample contained 0.1 wt% ^{19}F labeled, nonsticky dendritic nanoparticles with a hydrodynamic radius of 7.5 nm.[5,6] The overall sample volume was chosen as to not exceed the linear part of the magnetic field gradient. Sample temperature was kept at 293 K. DOSY experiments were performed by stepwise variation of the gradient pulse amplitude, while keeping the diffusion-observation time and gradient pulse duration constant. The attenuation of the NMR echo intensity as a function of increasing gradient amplitude is described by the Stejskal-Tanner equation $A = A_0\exp(-bD)$, where A is the echo intensity, D the self-diffusion coefficient (m^2/s) and $b = (\gamma\delta g)^2(\Delta - \delta/3)$, where γ is the gyromagnetic ratio of the observed nucleus (25.18×10^7 rad/(T s) for ^{19}F), g the magnetic field gradient amplitude (T/m), Δ the effective observation time (s) and δ the effective gradient pulse duration (s), where $\delta \ll \Delta$ (narrow gradient pulse approximation).[7] We used stimulated echo-based DOSY experiments with unipolar, ramped gradient pulses. In all experiments, an effective observation time Δ of 100 ms was used, and an effective gradient pulse duration δ of 5 ms. Gradient amplitude g was varied logarithmically between 0.10–9.60 T/m in 128 steps. The NMR signal was averaged between 16–64 times at each gradient amplitude, with a repetition time of 1 s. DOSY spectra were obtained through Fourier transformation of the stimulated echo for each gradient step and subsequent phasing using standard procedures. The signals in each of the resulting ^{19}F NMR spectra were integrated to obtain the attenuation curve.

Results and Discussion

Impact of CMC addition to BCMF on macroscopic and local viscosity

In Figure 1A, a cryo-SEM micrograph of microfibrils in the absence of CMC is presented, where the distribution of microfibrils is strongly heterogeneous. In Figure 1B, it can be seen that addition of CMC

(not visible) leads to a more homogeneous distribution of BC microfibrils over the available volume at the micron scale.

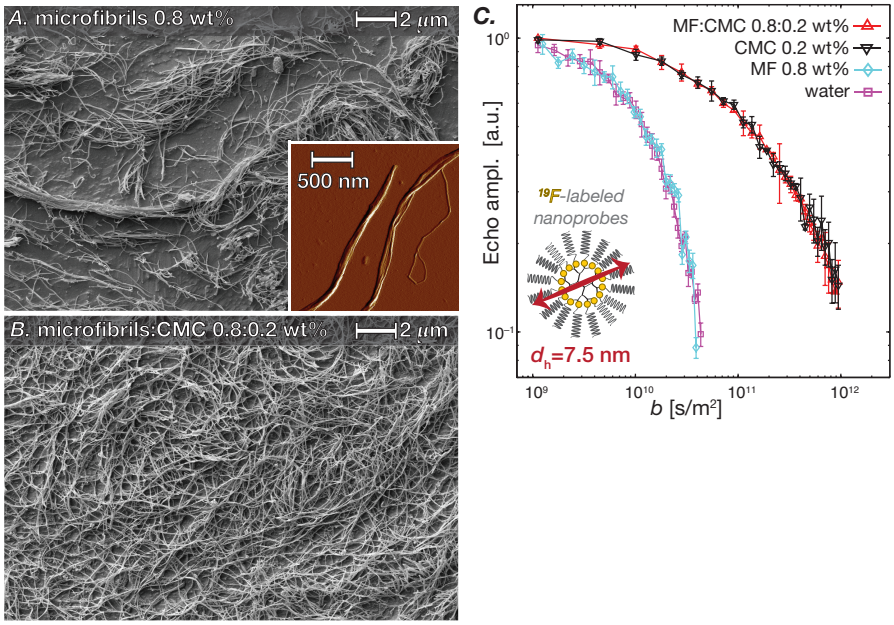

Figure S1-1. *A.* Cryo-SEM micrograph of a 0.8 wt% microfibrils (MF) dispersion. *Inset*: AFM image of a single microfibril (additional AFM images included in Figure S1-2) *B.* Cryo-SEM micrograph of a BCMF/CMC 0.8/0.2 wt% dispersion. *C.* PFG ^{19}F-NMR response curves of nanoprobes in water, MF 0.8 wt%, CMC 0.2 wt% and BCMF/CMC 0.8/0.2 wt%. These nanoprobes are ^{19}F-labeled PEGylated dendrimers with a diameter of 7.5 nm, as shown in the cartoon.

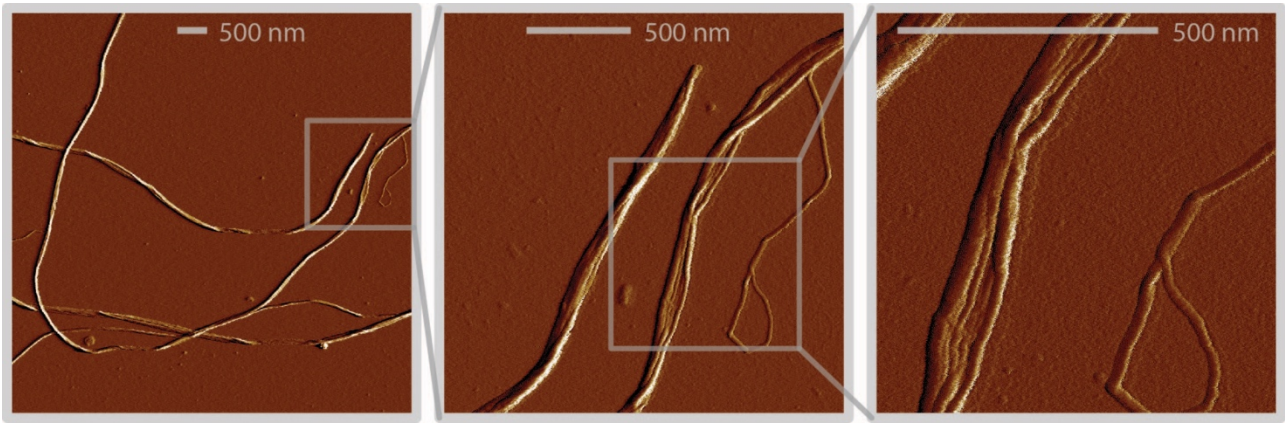

Figure S1-2. AFM micrographs of cellulose microfibrils (peak force error contrast). Individual fibers have a high aspect ratio (leftmost image). They are ribbon shaped, and can be seen twisting (middle image). The ribbons consist of laterally stacked elementary fibrils, which can individually protrude from the microfibrils (rightmost image).

As CMC is not visible in these images, we cannot see its spatial distribution and the manner in which it associates with the microfibrils. Therefore, we probe the apparent viscosity of the continuous phase *in situ* by measuring the mobility of nonsticky nanoprobes.[8,9] These nanoprobes are much smaller than the mesh size of the MF network and their mobility is therefore expected not to be influenced by the MF network. In Figure 1C, we can see PFG ^{19}F-NMR response curves of ^{19}F-labeled, PEGylated dendrimers with a hydrodynamic diameter of 7.5 nm.[5,6] The decay of echo amplitude A is plotted as function of b, which is proportional to the square of the pulsed magnetic field gradient intensity. The curves decay according to the Stejskal-Tanner equation $A = A_0 e^{-bD}$, where D is the particle self-diffusion coefficient.[7] The echo amplitude decay curves of the nanoparticles in water (bulk viscosity η = 1.0 mPa s) and in 0.8 wt% MFs overlap, demonstrating that the particles indeed probe the apparent viscosity of the continuous phase, which is not significantly different between both systems. It turns out that also the response curves of 0.2 wt% CMC (η = 5.8±0.3 mPa s) and 0.8/0.2 wt% BCMF/CMC overlap. We note that the CMC solution was microfluidized just like the BCMF/CMC dispersion to allow for unbiased comparison.

S1b. *Quantification of the amount of mobile CMC in BCMF/CMC dispersions*

This prompted us to quantify the amount of soluble CMC *in situ* in the dispersion, as well as in the supernatant upon centrifugation. The level of unbound CMC in BCMF/CMC dispersions was determined by two independent ^{1}H NMR methods. In one method the level of unbound CMC was determined *in situ* (Figure S1-3), and in the concentration range accessible to this method (>0.05 wt%) no significant difference between the amount of CMC put into the dispersion, and the amount of mobile CMC could be observed. Binding of CMC leads to decrease in mobility and hence disappearance of the NMR signal.

The level of mobile CMC in the dispersions was also determined by measuring the degree of recovery of CMC in the supernatant of centrifuged BCMF/CMC dispersions (Figure S1-4). This method can access lower CMC levels (0.01-0.07 wt%) and shows near-complete recovery of CMC in the supernatants of BCMF/CMC dispersions. We verified that no BCMF had remained in the supernatant by comparing the ^{1}H NMR spectra of the Seaman hydrolysates (Figure S1-5). The ratio of glucose to carboxyl-glucose was similar in a pristine CMC solution and the supernatant of a BCMF/CMC dispersion.

The results of both the diffusometric and spectroscopic approaches show that within experimental

error (5%) the amount of mobile CMC equals the dosed concentrations of respectively 0.2 and 0.8 wt%. These results consistently indicate that a smaller (<5%) fraction of CMC is adsorbed to the BC microfibrils than previously estimated[1].

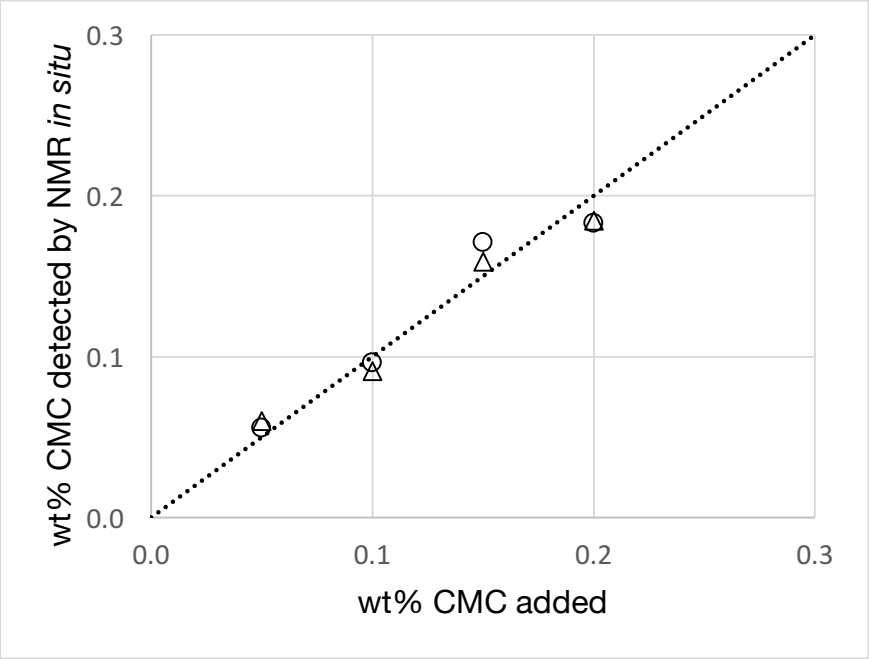

Figure S1-3. The amount of mobile CMC in BCMF/CMC dispersions was measured *in situ* from the ^{1}H NMR signal intensity of CMC between 2.94–4.28 ppm on a Bruker Avance III spectrometer operating at 600 MHz using the Eretic signal as an internal standard. The lineshape of CMC ^{1}H NMR resonances in the BCMF/CMC dispersions was similar to that in pristine CMC solutions. Circles and triangles represent experimental repetitions. The concentration of mobile CMC was calculated from a concentration response curve of CMC solutions with known concentrations.

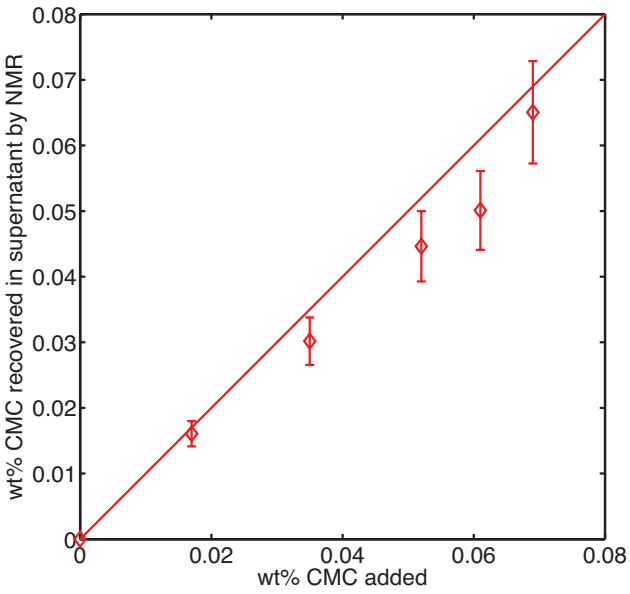

Figure S1-4. Amount of mobile CMC in BCMF/CMC dispersions as determined from CMC recovery of CMC in the supernatant upon centrifugation. The amount of CMC added into the dispersions is plotted against the content in the supernatant. CMC content was determined by quantitative monosaccharide analysis upon Saeman hydrolysis. Samples are measured in 14 wt% D_2SO_4 in D_2O on a Bruker Avance III spectrometer operating at 600 MHz. The glucose anomeric proton peaks [δ 4.8-3.9 ppm] and carbomethoxyl CH_2-peaks [δ 3.58-3.54 ppm] are used for the quantification. The glucose:carbomethoxyl molar ratio (4:1) remains constant for all the BCMF/CMC-dispersions, indicating that no additional glucose from BCMF is introduced in the supernatant.

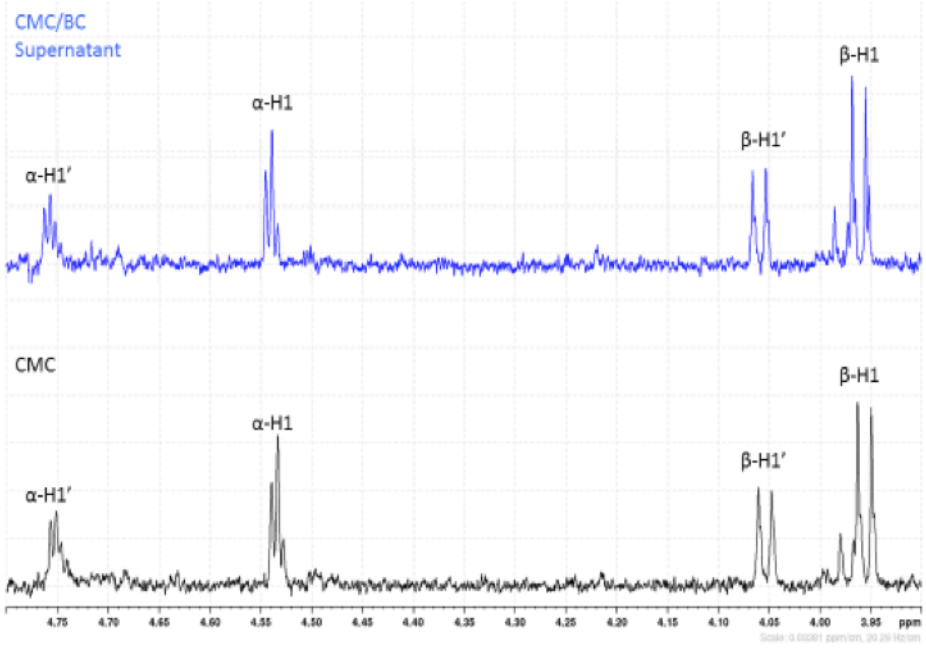

Figure S1–5 Anomeric region of the 600 MHz ^{1}H-NMR spectrum of two hydrolysed CMC-containing systems in 14% D_2SO_4 in D_2O. In this spectral area, the anomeric protons of glucose (α-H1 + β-H1) and carboxymethylated glucose (α-H1 + β-H1) are present. The top spectrum (hydrolysed supernatant of BCMF/CMC) is not significantly different from the bottom spectrum (hydrolysed pristine CMC solution), implying that no compound besides CMC is present in the supernatant after centrifugation of the BCMF/CMC dispersion.

S2. *Uncorrected flow profiles in cone-plate geometry*

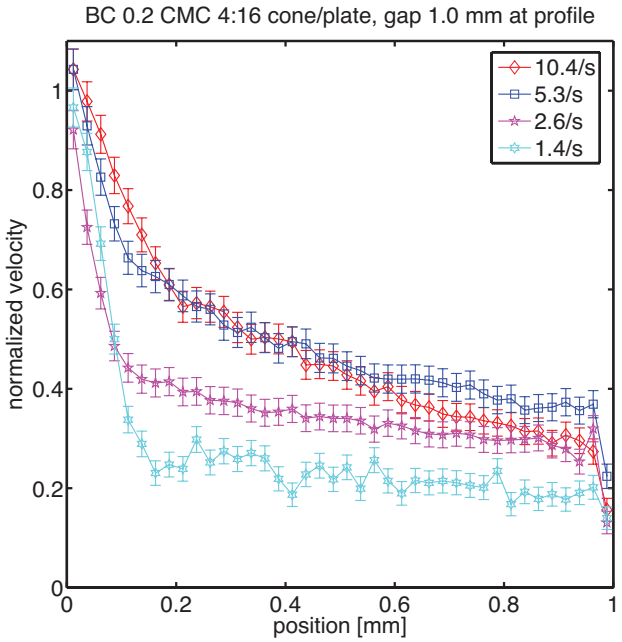

Figure S2-1. Uncorrected flow profiles in cone/plate geometry, where slippage at the (smooth) plate is visible. This was subtracted by extrapolation of the last five pixels at the plate and subtracting the slip velocity.

S3. *Solution of the nonlocal model for Couette flow (homogeneous stress)*

The nonlocal model (ref 10):

$f(z)=f_{\text{bulk}}+\xi^2\frac{\partial^2 f(z)}{\partial z^2}$, where $f(z)=\frac{1}{\eta(z)}=\frac{\dot{\gamma}(z)}{\sigma(z)}$

For flows between two parallel plates (Couette flow), where the stress throughout the liquid is homogeneous ($\sigma(z)=\sigma_0$), the solution to this equation is:

$$\sigma_0 f(z)=\sigma_0 f_{\text{bulk}}+A\cosh\left(\frac{z}{\xi}\right)+B\sinh\left(\frac{z}{\xi}\right)$$

Condition 1: $A=\sigma_0(f_{z=0}-f_{\text{bulk}})$

$\sigma_0 f(z)=\dot{\gamma}(z)$, and between parallel plates the local shear rate $\dot{\gamma}(z)=\frac{\partial v(z)}{\partial z}$, so that integration over z gives:

$$v(z)=\sigma_0 f_{\text{bulk}}z+\sigma_0(f_{z=0}-f_{\text{bulk}})\xi\sinh\left(\frac{z}{\xi}\right)+B\xi\cosh\left(\frac{z}{\xi}\right)+C$$

Condition 2 from z=0: $C=v(0)-B\xi$, so that:

$$v(z)=v(0)+\sigma_0 f_{\text{bulk}}z+\sigma_0(f_{z=0}-f_{\text{bulk}})\xi\sinh\left(\frac{z}{\xi}\right)+B\xi\left[\cosh\left(\frac{z}{\xi}\right)-1\right]$$

Condition 3 from z=h:

$$B=\frac{v(h)-v(0)-\sigma_0 f_{\text{bulk}}h-\sigma_0(f_{z=0}-f_{\text{bulk}})\xi\sinh\left(\frac{h}{\xi}\right)}{\xi\left[\cosh\left(\frac{h}{\xi}\right)-1\right]}$$

So that the velocity profile is:

$$v(z)=v(0)+\sigma_0 f_{\text{bulk}}z+\sigma_0(f_{z=0}-f_{\text{bulk}})\xi\sinh\left(\frac{z}{\xi}\right)+\frac{v(h)-v(0)-\sigma_0 f_{\text{bulk}}h-\sigma_0(f_{z=0}-f_{\text{bulk}})\xi\sinh\left(\frac{h}{\xi}\right)}{\cosh\left(\frac{h}{\xi}\right)-1}\left[\cosh\left(\frac{z}{\xi}\right)-1\right]$$

In the absence of slip and if h is the distance between the plates, $v(h)$ is equal to the velocity of the moving wall and $v(0)=0$.

S4. *Apparent wall slip*

Experimental procedures. Experiments were performed on an Anton Paar Physica MCR301 rheometer equipped with a PP geometry with a diameter of 4 cm. The gap size was calibrated from the viscosity of paraffin oil according to procedures described in refs [11,12]. Strain controlled flow curves of BCMF/CMC 0.20/0.05 wt% were measured with gap widths of 1.1 and 0.8 mm, after pre-shearing the sample at 200 s^{-1} for 3 minutes. The shear rate was decreased from 2×10^{2} to 2×10^{-3} s^{-1} over the course of 1h.

Results and discussion. The presence of (apparent) wall slip is determined by measuring flow curves in PP geometry at different plate separations. If we assume the apparent slip velocity v_s to be a function of stress alone, the apparent shear rate in parallel plates geometry has contributions from both the true shear rate and slippage: $\dot{\gamma}_{app}=\dot{\gamma}(\sigma)+\frac{2v_s(\sigma)}{d}$, where d is the separation between the plates. We can determine $v_s(\sigma)$, by measuring the steady state flow curves $\dot{\gamma}_d(\sigma)$ at two different gap widths d (Figure S4-1, for BCMF/CMC 0.20/0.05 wt%). In this depiction we indeed observe minor but significant differences between the flow curves. The slip velocity follows from $v_s(\sigma)=\frac{\dot{\gamma}_{d_1}(\sigma)-\dot{\gamma}_{d_2}(\sigma)}{2\left(1/d_1-1/d_2\right)}$.[13] We observe apparent wall slip throughout a significant part of the flow curves, also at shear rates higher than the critical shear rate.

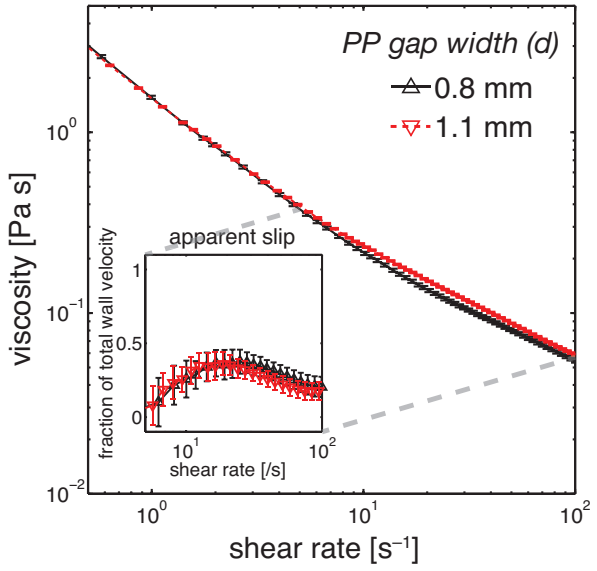

Figure S4-1. Gap-dependent viscosity differences in BCMF/CMC 0.20/0.05 wt%. The flow curves were measured under strain-controlled conditions over the course of 1h. The contribution of the apparent slip to the total wall velocity (inset) is given by $v_s(\sigma)/(d\dot{\gamma}_d(\sigma))$.

References

1 S. J. Veen, P. Versluis, A. Kuijk and K. P. Velikov, *Soft Matter*, 2015, 1–6.
2 H. Yamamoto and F. Horn, *Cellulose*, 1994, **1**, 57–66.
3 C. H. Haigler, A. R. White, R. M. Brown and K. M. Cooper, *J. Cell Biol.*, 1982, **94**, 64–69.
4 D. Alsteens, V. Dupres, S. Yunus, J.-P. Latgé, J. J. Heinisch and Y. F. Dufrêne, *Langmuir*, 2012, **28**, 16738–16744.
5 D. W. de Kort, J. P. M. van Duynhoven, F. J. M. Hoeben, H. M. Janssen and H. Van As, *Anal. Chem.*, 2014, **86**, 9229–9235.
6 D. W. de Kort, W. H. Rombouts, F. J. M. Hoeben, H. M. Janssen, H. Van As and J. P. M. van Duynhoven, *Macromolecules*, 2015, **48**, 7585–7591.
7 E. O. Stejskal and J. E. Tanner, *J. Chem. Phys.*, 1965, **42**, 288–292.
8 D. W. de Kort, J. P. M. van Duynhoven, H. Van As and F. Mariette, *Trends Food Sci. Technol.*, 2015, **42**, 13–26.
9 N. Bourouina, D. W. de Kort, F. J. M. Hoeben, H. M. Janssen, H. Van As, J. Hohlbein, J. P. M. van Duynhoven and J. M. Kleijn, *Langmuir*, 2015, **31**, 12635–12643.
10 J. Goyon, A. Colin, G. Ovarlez, A. Ajdari and L. Bocquet, *Nature*, 2008, **454**, 84–87.
11 J. Kramer, J. T. Uhl and R. K. Prud'homme, *Polym. Eng. Sci.*, 1987, **27**, 598–602.
12 O. Kravchuk and J. R. Stokes, *J. Rheol.*, 2013, **57**, 365–375.
13 A. Yoshimura and R. K. Prud'homme, *J. Rheol.*, 1988, **32**, 53–67.